

# Study of silicon photomultipliers for use in neutron decay experiments

D. Dubbers

*Physikalisches Institut, Heidelberg University, Im Neuenheimer Feld 226, 69120 Heidelberg, Germany*

*Dated:* 10 September 2020

*Keywords:* Neutron decay,  $\beta$  spectroscopy, electron detector, plastic scintillator, SiPM

*E-mail address:* dubbbers@physi.uni-heidelberg.de

## *Abstract*

The possible use of silicon photomultipliers (SiPMs) for scintillator readout in neutron  $\beta$  decay experiments is investigated. Various theoretical and experimental tools are developed for this purpose, including a virtual image model of scintillator readout, a method to extract the photoelectron yield from an electron conversion line in the presence of electron backscattering, and a reflectometer setup to quantify photon losses in scintillators. Experimental and theoretical photoelectron yields are obtained as a function of the number of SiPMs installed, and a procedure to handle the extreme rates of dark counts typical for SiPMs is proposed. In  $\beta$  spectroscopy, so the conclusion, scintillator readout with SiPMs may be a viable alternative to conventional readout with photomultipliers, and will significantly improve energy resolution of plastic scintillators. Our first application of SiPMs will be in a time-of flight experiment on electron backscattering from the detectors used in neutron decay experiments.

## **1. Introduction**

The weak interaction parameters obtained from neutron  $\beta$  decay  $n \rightarrow p^+ e^- \bar{\nu}_e$  are needed in several fields of physics and astrophysics, see the reviews [1], [2], [3], [4]. In recent years, the precision of neutron decay data has considerably improved, as documented by the Particle Data Group (PDG), see Ref. [5] and preceding editions. With it, the demand on the quality of future neutron decay instruments has also increased.

Many neutron decay experiments use plastic scintillators for the spectroscopy of the decay electrons. Recent examples are the instruments PERKEO at ILL [6], UCNA at LANL [7], aCORN [8] and emiT [9] at NIST, the *R* instrument at PSI [10], the upcoming PERC at FRM-II [11] and the projected BRAND [12]. In comparison to silicon detectors,

plastic scintillators have thinner dead layers, lower backscattering coefficients, less background sensitivity, and faster response time, which outweighs their lower energy resolution.

All these neutron decay instruments use conventional photomultiplier tubes (PMTs) for scintillator readout. In addition, we used PMT readout of plastic scintillators in several auxiliary experiments, be it to measure the point spread function of the electrons after magnetic transport [13], [14], or the scintillator response function with an electron time-of-flight (ToF) method [15]. It should be helpful if one could replace the clumsy and magnetic-field sensitive PMTs in these experiments by silicon based photon detectors, such as the so-called silicon photomultipliers or SiPMs.

SiPMs are solid state photodetectors composed of a large number of tiny single photon avalanche diodes, each acting as a Geiger-Müller counter, whose binary signals directly count the number of photons. In recent years, SiPMs have found many applications, in particular in high energy-, astro-, and medical physics. For reviews on properties and characterization of SiPMs see Refs. [16], [17], [18]. Their use in nuclear and particle physics is reviewed in [19], and applications in high-precision  $\gamma$  spectroscopy are described in [20], [21].

The advantages of SiPMs over PMTs are their small size, weight, and cost, their low operating voltage, and their insensitivity to magnetic fields. They have similar efficiency as PMTs with respect to single photon detection, signal rise time, and linearity. Disadvantages of SiPMs are their high rate of dark counts, and correlated noise like after-pulsing and optical cross talk. The present article will study, both in theory and experiment, the possible use of SiPMs in neutron physics.

The paper is organized as follows. To define our needs, Section 2 sketches the intended use of SiPMs, both short term in an auxiliary experiment on electron backscattering, and long term in neutron decay studies. Section 3 introduces a method of virtual images to model the readout of scintillators by SiPMs. Our simple test setup is described in Section 4. Section 5 treats the derivation of the photoelectron yield from conversion electron spectra, while Section 6 shows how the effects of electron backscattering in these spectra can be corrected. To reduce the number of free parameters in the subsequent studies, photon absorption and reflection losses were measured, as described in Section 7. Section 8 then compares theory and experiment of the

photoelectron yield as a function of the number  $N$  of SiPMs installed. This is done for two different scintillator sizes, in order to enable extrapolation to larger scintillators. Section 9 develops a strategy for suppressing dark counts and correlated noise that become extreme for larger  $N$ , which is followed by an outlook on the suitability of SiPMs in neutron decay experiments.

## 2. Planned SiPM application

Our first application of SiPMs will be in an experiment on electron backscattering. While, in the neutron decay experiments listed above, electron backscattering effects are suppressed by various means, second order effects still contribute considerably to the error budget [22], [23], [24]. Electron backscattering from plastic scintillators had been studied before, limited however to normal incidence [25] or to an integrated angular range [26]. The planned experiment will cover all relevant electron variables in a single run, including crazing angles  $\theta_1 \approx 90^\circ$  or  $\theta_2 \approx 90^\circ$  and backscattering at low energies where Monte Carlo simulations [27], [28] still have problems.

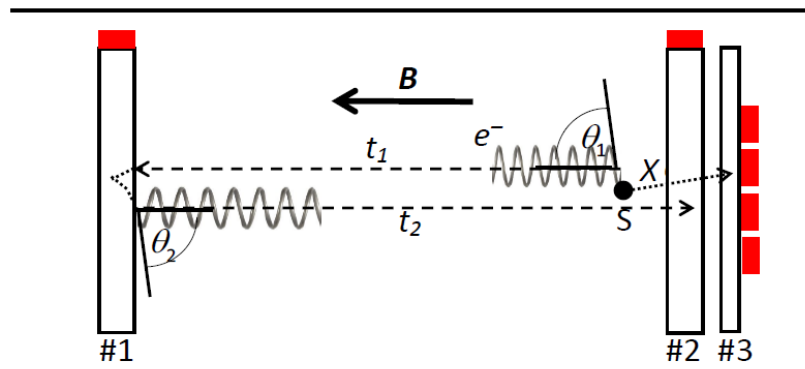


Fig. 1. Arrangement of SiPMs (red) in a complete experiment on electron backscattering. The electrons, emitted by the source  $S$  under angle  $\theta_1$ , gyrate about the uniform magnetic field  $B$  until they reach detector #1 after a time-of-flight  $t_1$ . The electrons backscattered under angle  $\theta_2$  reach detector #2 after a ToF  $t_2$ . Both electron detectors are plastic scintillators. Time zero is given by an x ray detected in a LaBr<sub>3</sub> scintillator #3. For details see text.

Fig. 1 shows the setup of the planned backscatter experiment. An electron is backscattered from scintillator #1 and is registered in scintillator #2. In the uniform guide field  $\mathbf{B}$ , the angle of emission  $\theta_1$  from source S of is the same as the angle of incidence on #1, and is derived with standard formulae from its known initial energy  $E$  and its measured ToF  $t_1$ . Similarly, the angle of emission  $\theta_2$  of the backscattered electron is derived from its measured residual energy  $E_2$  and ToF  $t_2$ . The measured energies deposited in the 5 mm thick scintillators #1 and #2 sum up to  $E_1 + E_2 = E$ .

The ToF start pulse can be supplied by a prompt photon from a  $\beta$ - $\gamma$  emitter or from a conversion electron plus x ray emitter. In the case of  $^{207}\text{Bi}$  (30 y), a 1.0 MeV conversion electron is accompanied by x rays from the K shell of mean energy 77 keV, which is registered in the  $\text{LaBr}_3$  crystal #3. The electrons detected in #2 do not reach #3, while the x rays cross #2 with almost no losses. The ratio of triple coincidences (#1,#2,#3) to double coincidences (#1,#3) will give the backscattering coefficient as a function of the parameters  $E, E_1, \theta_1, \theta_2$  all in one single run. For a given electron conversion line,  $E$  is known and hence overdetermined, while in the  $\beta$ - $\gamma$  case it is measured as  $E = E_1 + E_2$ .

For the detector arrangement of Fig. 1, with 20 ns coincidence time and a backscattering coefficient of 10%, 1000 decays at 1.0 MeV will give 12 true and 0.2 random triple coincidences (#1,#2,#3), and 120 true and 0.14 random double coincidences (#1,#3). Gamma and electron backgrounds are negligible both in these rates. In particular, triggering with an x ray guarantees that there is no coincident background from the alternative Auger electron transition. The angular sensitivity obtained with this method was discussed in Sections 4 and 5 of [29].

In our previous studies, acrylic light guides had transported the photons from a scintillator, installed inside a superconducting solenoid (PERKINO), to an external PMT. Evidently, in the setup of Fig. 1 there is no room for PMT readout of all scintillators. If done with the 0.3 m long PERKINO magnet, a timing uncertainty of below 200 ps would be required. In the ToF experiment of Ref. [15] we had reached this value, but this may be challenging for the full system of Fig. 1, whence the experiment may better be done in the long uniform field region of the upcoming PERC instrument.

If this goes well, next the application of SiPMs in neutron decay experiments will be of interest. Neutron  $\beta$  decay experiments often search for new physics beyond the left

handed V–A standard model. Often this requires precise measurements of spectral shapes, for instance to search for scalar S or tensor T admixtures or for right handed V+A currents in the neutron's decay amplitude [30], [31], [32]. Therefore, we also want to find out whether one can improve electron energy resolution when using SiPM readout.

Neutron decay volumes have typical cross sections of one decimeter. From this decay volume, a magnetic guide field transports the decay electrons to plastic scintillator plates of at least similar size, which are read out over their four edges by light guides coupled to PMTs. The question then is whether these edges can instead be fully covered with SiPMs. At first sight, the typical dark rates of SiPMs of 100 kHz per mm<sup>2</sup> look rather prohibitive.

### **3. Modelling of the scintillator-SiPM system**

In a plastic scintillator, photons generated by electron irradiation are repeatedly reflected from the scintillator's inner surfaces, or from additional reflector foils, until they are absorbed in a detector attached to the scintillator. The upper part of Fig. 2 shows a scintillator plate (or "tile") with an SiPM attached to one of its lateral faces. For a critical angle near 45°, total photon reflections almost never occur at these edges [33]. Therefore, except for an opening for the SiPM, they must be covered by reflecting foils. In contrast, the larger uncovered faces through which the electrons enter are totally reflecting from the inside for angles beyond the critical angle. At first sight, an ideal gas escaping from a vessel through a leak resembles this process, but the well-known formulae for this case do not apply because the photons in the scintillator are not an ergodic system in thermal equilibrium.

There are many publications on ray tracing Monte Carlo simulations of scintillators, for a comprehensive review see [34]. For the frequent case of scintillators in the shape of a rectangular plate or parallelepiped, photon trajectories were also investigated algebraically, see [33] and [35]. In this paper, a method of virtual images is used, apparently for the first time. For two dimensions, the method is visualized in the lower part of Fig. 2. In the center is the scintillator plate in red, surrounded by a set of virtual images in gray as seen through the mirroring lateral faces.

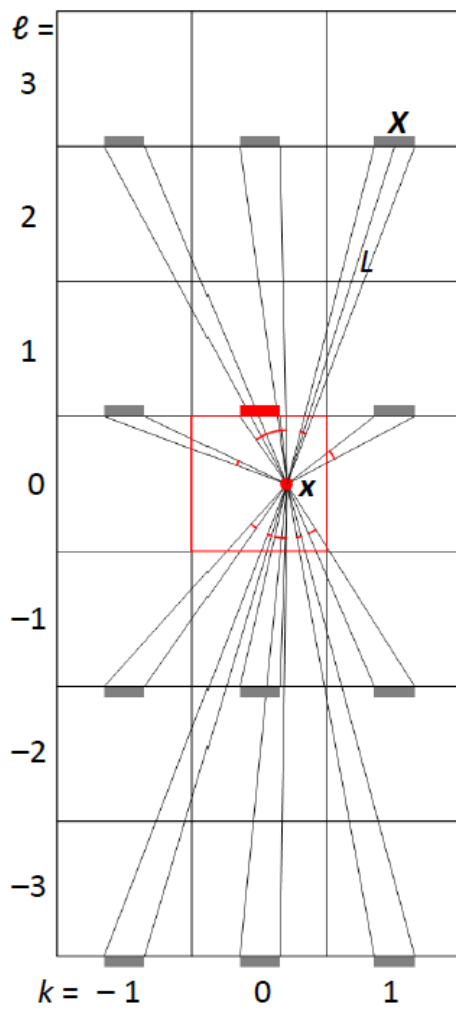
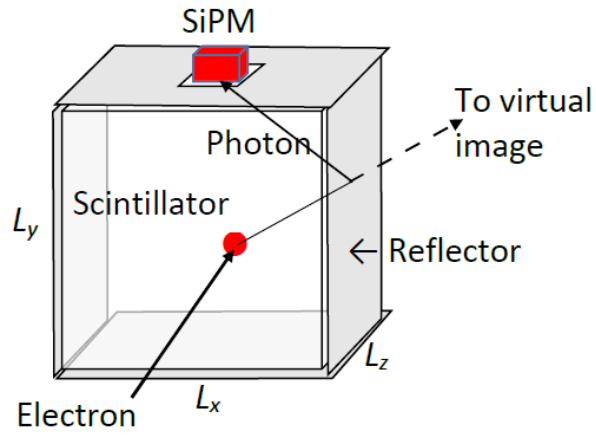


FIG. 2. Photon trajectories in a scintillator-SiPM system. Upper part: A scintillator plate with lateral reflectors and with a SiPM (red) attached to one of its lateral faces. Lower part: The same system treated by the method of virtual images. The real system in the center (red) is surrounded by its virtual images (gray), as mirrored by the reflectors. The arcs (red) around the emission point indicate the angular ranges under which the photons can be detected.

The detection probability for a photon, generated at position  $\mathbf{x}$  within the scintillator, is obtained from the sum of solid angles under which the real and virtual SiPMs appear when seen from position  $\mathbf{x}$ . In the figure these angles are indicated by the circular segments drawn around  $\mathbf{x}$ . When a detector, real or virtual, is hit by the photon, it frequently shadows some of the more distant virtual detectors. – In this way, the problem of light evolution in a scintillator plate is reduced to a simple addition of angles.

On their way to the detectors, photons will suffer various losses. Let, in three dimensions, the scintillator tiles be numbered along  $x, y, z$  by successive integers  $k, \ell, m$ , with the central real tile at  $k = \ell = m = 0$ , as indicated in the figure. The distance of a virtual tile to the real tile then is given by  $|k|, |\ell|, |m|$ . On its way to a virtual detector at position  $\mathbf{X}$ , the photon may be lost due to an imperfect reflectivity  $R_f < 1$  of the reflector foils or  $R_t < 1$  of the totally reflecting surfaces. The mean loss on the reflector foils then is  $1 - (R_f)^M$ , with the number of reflections  $M = |k| + |\ell|$  when emission is into the half-space above the photon emission point with coordinate  $y$ , and  $M = |k| + |\ell| - 1$  otherwise. The mean loss on the two large totally reflecting faces of the tile is  $1 - (R_t)^{\Delta m}$ . In addition there are mean absorption losses of size  $1 - \exp(-L / \lambda)$ , where  $L = |\mathbf{X} - \mathbf{x}|$  is the length of the photon's trajectory and  $\lambda$  the scintillator's absorption length.

In the following we denote the photoelectron yield (p.e./MeV) shortly as yield  $R$ . In Figs. 3 to 5,  $R$  is calculated as a function of various parameters, and is arbitrarily set to 100 p.e./MeV in the middle of each abscissa. The plastic scintillator has refractive index  $n = 1.58$ , critical angle  $\theta_c = \arcsin(1 / n) = 39^\circ$ , and dimensions  $20 \times 20 \times 5 \text{ mm}^3$ , same as used in the experiments described later on. The photons start in the middle ( $\mathbf{x} = 0$ ) of the scintillator with transmission parameters  $R_f = R_t = 0.95$  and  $\lambda = 100 \text{ cm}$ , while the SiPMs have an area of  $3 \times 3 \text{ mm}^2$  and are positioned in the center of the scintillator's lateral face, all unless stated otherwise.

Fig. 3 shows the yield  $R$  as a function of the various photon transmission parameters. While  $R_f$  and  $R_t$  can differ from each other, their dependence on  $R$  is very similar. Fig. 4 shows  $R$  as a function of detector position  $x_d$  and of photon start position  $x$ . The small variations of  $R$  are no artifacts: they disappear when photon losses are switched off. Fig. 5 shows  $R$  in dependence of the number  $N$  of SiPMs, installed one next to the other.

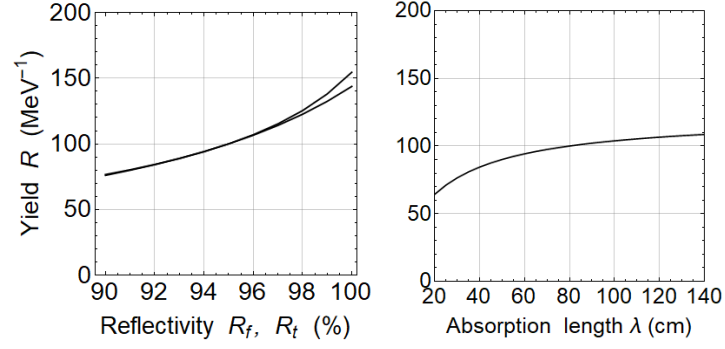


Fig. 3. Sensitivity of photoelectron yield  $R$  (in p.e. per MeV) to various photon loss mechanisms. Left:  $R$  as a function of reflectivity  $R_f$  of the reflector foils (lower curve) and of total reflectivity  $R_t$  of the inner scintillator faces (upper curve). Right:  $R$  as a function of photon absorption length  $\lambda$ .

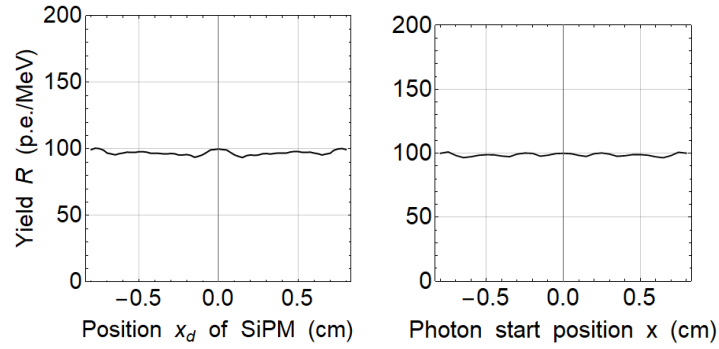


Fig. 4. Position sensitivity of yield  $R$ . Left:  $R$  as a function of detector position  $x_d$ . Right:  $R$  as a function of photon start position  $x$ .

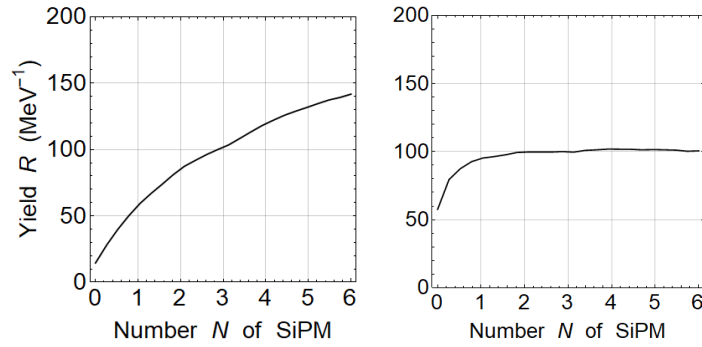


Fig. 5. Yield  $R$  in dependence of the number  $N$  of SiPMs. Left: with photon losses. Right: without photon losses,  $R$  is independent of  $N$  (here for  $N \geq 1$ ).

The number of virtual images needed in the calculation of  $R$  can be checked by setting all photon losses to zero. In this case, even a single SiPM will finally capture all photons emitted under  $\theta < \theta_c$ , with a solid angle of photon acceptance of  $\omega / 4\pi = (1 - 1/n^2)^{1/2}$

$=0.77$ . The number of virtual images must then be increased until the yield  $R(N)$  becomes sufficiently independent of  $N$ , at least for  $N \geq 1$ . This is the case when  $k_{max} = \ell_{max} \approx 40$  as shown on the right of Fig. 5 (while, for given  $k$  and  $\ell$ ,  $m_{max}$  is determined by  $\theta_c$ ).

Scintillator tiles of centimeter size with SiPM readout are also foreseen in various high-energy experiments, for instance in the mu3e project at PSI with about 6000 units in its first phase [36], [37], in the PANDA project at GSI with 10 000 units [38], and in the CALICE project at CERN with up to 20 000 units [39].

#### 4. Measurement tools

For the measurement of electron spectra and photoelectron yields with SiPMs, the following equipment was used. The plastic scintillators were square tiles of size  $L_x = L_y = 20$  and 40 mm and thickness  $L_z = 5$  mm (BC400 from Saint-Gobain). They were coupled to blue-sensitive SiPMs, each with about  $10^4$  pixels of area  $25 \times 25 \mu\text{m}^2$  each, assembled to a chip of area  $3 \times 3 \text{ mm}^2$  with a fill factors of about 70% (KETEK PM3325-WB).

The SiPM chips were not glued to the plastic scintillator, so they could be reused. Instead they were pressed to lateral faces of the tiles with a mild force of several Newtons, their optical contact being assured by a thin layer of silicon grease of refractive index  $n = 1.41$  (Rhodosil PÂTE 7), while the glass of the SiPM entrance window has  $n = 1.52$ . Without grease, the yield  $R$  decreased by 30%. The SiPMs are rather robust but can break under stronger pressures, although they may survive even breakage. They also forgive wrong polarity of the voltage applied, but overvoltage and operation under ambient light must be avoided. The lateral faces of the scintillator tiles were covered with reflector foils of up to nominal 99% reflectivity (Vikuti Enhanced Specular Reflector 3m ESR from 3m Optical Systems. N.B.: Bids for one square foot of identical 3m-ESR foils vary from lower two-digit to almost four-digit Euro amounts). Square holes of 3.3 mm lateral size were punched into the foils at the positions of the SiPMs, see top of Fig. 2. When aluminized mylar foils were used instead, the yield  $R$  decreased by 17%.

The electronics used is simple: a detector voltage, usually 2.5 to 5 V above the breakthrough voltage of 24.5 V, was applied to the SiPM through a series resistor of 10 k $\Omega$ , with a parallel capacitance of 100 nF to ground. The signals were read out over a load resistor of 3 k $\Omega$  and were decoupled from the circuit by a capacitance of 100 nF. These values can be varied over a wide range without affecting the signals, because their

10% to 90% rise time of 10 ns and decay time of 90 ns are due to the internal structure of the SiPM. The typical signal amplitude of a single SiPM coupled to the 20×20×5 mm<sup>2</sup> tile is 50 mV for 1 MeV electron energy. When several SiPMs are installed in parallel, the detector capacity and with it the decay time of the signal increases, while its amplitude changes only marginally. These signals then passed a timing filter amplifier (Ortec TFA 472) with integration constant set to 200 ns, with no need for a preamplifier. The spectra were registered in a multichannel analyzer (Pitaya STEMLab 125-14).

A nearly point-like <sup>207</sup>Bi source was dried onto an about 5 μm thick foil of aluminized mylar. The source's K-conversion electron energies are  $E = 0.98$  MeV and 0.48 MeV, with intensity ratio of 84.1 to 8.8. The electrons reached the scintillator from a distance of 12 mm through an orifice of 12 mm diameter, made from a sheet of 1.7 mm copper, covered towards the scintillator with 0.4 mm cardboard to absorb secondary electrons released by the unconverted γ rays.

## 5. Measurement of photoelectron yield $R$

A β spectrum is a histogram of the photoelectron yield  $R$  over electron energy  $E$ . Electron detectors can be calibrated with monoenergetic electrons of known energy. For scintillation detectors, the linewidth is usually dominated by the statistical fluctuations of the number  $n$  of detected photoelectrons, which we assume to be large enough that the spectrum can be approximated by a Gaussian,

$$\frac{dn}{dE} = \frac{n_0}{\sqrt{2\pi}\sigma^2} \exp\left[-\frac{(E - E_0)^2}{2\sigma^2}\right], \quad (1)$$

with variance  $\sigma^2$  and full width at half maximum  $\text{FWHM} = 2\sqrt{2\ln 2} \sigma$ . With  $\sigma / E_0 = 1 / \sqrt{\langle n \rangle}$ , the mean number of photoelectrons is  $\langle n \rangle = (E_0 / \sigma)^2$ , and the photoelectron yield per MeV is  $R = \langle n \rangle / (E_0 / \text{MeV})$ .

In β spectroscopy there is no need for spatial resolution, and with SiPMs as light detectors, the unit signals from the individual pixels are simply added up. In a SiPM, the dark signals cannot be distinguished from the true one-photon signals, whose energy is  $E_{1phe} = R^{-1}$ , for example,  $R = 200$  p.e./MeV gives  $E_{1phe} = 5$  keV. These dark counts then must be suppressed by a discriminator threshold.

When there is no magnetic field to guide the electrons from a distant source to the scintillator, the γ rays from the <sup>207</sup>Bi source irradiate the scintillator at a large solid angle

and produce a background of 40% of the total rate. This background was measured separately with the electrons absorbed in a sheet of 5 mm polyethylene, both before and after data taking, and was subtracted from the spectrum.

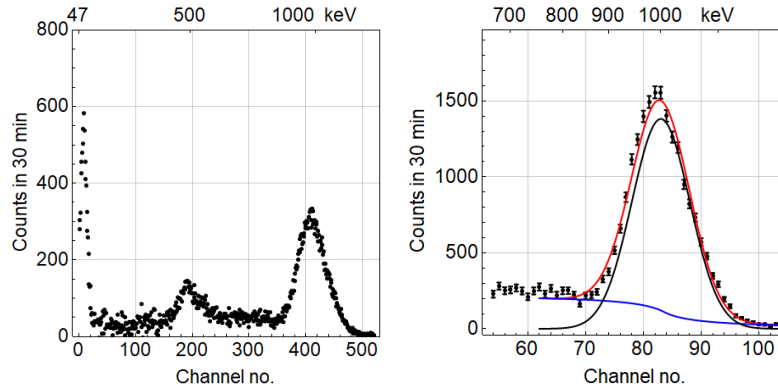


Fig. 6. Electron spectrum from the  $^{207}\text{B}$  source. Left: The two conversion peaks plus the Auger peak at low energy. Right: Simultaneous fit (red) to the Gaussian (black) plus the backscatter fraction (blue) from Eq. (2) below (data are summed up over five channels). From the fitted width the yield  $R$  is obtained, as described in the text.

Fig. 6 shows a background reduced  $^{207}\text{Bi}$  electron spectrum, taken with two SiPMs installed on opposite lateral faces of the  $20\times 20\times 5\text{ mm}^3$  scintillator, with an overvoltage of 5.5 V. The left panel shows the total spectrum with the two conversion peaks at 1.0 MeV and 0.5 MeV and the Auger K-electron peak at 63 keV. The zero offset of the spectrum is 13 channels or  $-47\text{ keV}$ . On the right is Gaussian a fit to the 1.0 MeV peak, based on the well-known electron conversion data. From its 11.8(3)% FWHM, the yield is determined to  $R = 281(7)\text{ p.e./MeV}$ , where the one sigma errors in the last digit is given in parentheses. This is to be compared to  $R = 300\text{ p.e./MeV}$  reached in our PERKINO measurements with tiles of similar size, coupled with a light guide of 4 cm diameter to a PMT of 2" diameter.

In addition, the  $^{207}\text{Bi}$  x-ray peak needed for the ToF backscatter project discussed in Section 2 was measured with an encapsulated  $\text{LaBr}_3(\text{Ce})$  crystal ( $20\times 20\times 3\text{ mm}^3$ ,  $5.1\text{ g/cm}^3$ , from Ost Photonics Co.). The hygroscopic crystal had a 1 mm Al window and was read out with a conventional PMT. The 77 keV x-ray K-line had 34 keV FWHM, corresponding to  $R = 360\text{ p.e./MeV}$ , and was almost background-free. It is hence well suited to give the start pulse in the backscatter project. Furthermore, the combined  $^{207}\text{Bi}$  electron and x ray

spectrum was taken with a bare LYSO crystal (Lutetium-yttrium oxyorthosilicate, 20×20×1 mm<sup>3</sup>, 7.4 g/cm<sup>3</sup> from Shalomeo Co.), which can be used as an alternative x-ray or electron detector.

## 6. Elimination of backscatter effects

In Fig. 6, some residual intensity remains between the two conversion peaks, essentially due to electron backscattering from the scintillator. The yield  $R$  obtained from the fit then depends on how these counts are continued under the measured peaks: the larger the deduced backscatter fraction, the smaller the width of the remaining conversion peak. As we want to know the width of the peak (and with it the yield  $R$ ) without energy shifts, the backscatter fraction under the peak must be subtracted. Unfortunately, its shape is unknown and cannot be determined numerically, as the tiny energy shifts involved are difficult to simulate (hopefully, our future experiment will provide the data needed for this).

The problem can, however, be solved empirically. The residual backscatter spectrum is roughly constant for energies below and zero (or equally constant) above the conversion peak, see Fig. 6. Under the peak, the backscatter spectrum is expected to be a continuously decreasing function of  $E$ . Hence this function must have an inflection point under the peak. A simple function fulfilling this requirement is

$$f(E) = \frac{1}{2} f_0 \left( 1 - \frac{E - E_{inv}}{w + |E - E_{inv}|} \right), \quad (2)$$

which is added to the well-known fit function for the undisturbed 1.0 MeV conversion line. With the three parameters: amplitude  $f_0$ , inflection point  $E_{inv}$ , and width  $w$ , Eq. (2) covers practically all shapes that the residual spectrum under the peak can reasonably assume, from an almost linear decrease for a large  $w$  to a step function for  $w = 0$ .

To our surprise, a six parameter fit to the data ( $f_0$ ,  $E_{inv}$ ,  $w$  from Eq. (2) and  $n_0$ ,  $E_0$ ,  $\sigma$  from Eq. (1)) has the result shown in red on the right panel of Fig. 6. The inflection point  $E_{inv}$  coincides within a few percent with the conversion energy  $E_0$ , and the width  $w$  is comparable to the line's FWHM. This means that beyond the peak's maximum, the backscatter fraction approximately follows the downward shape of the conversion peak, that is, it is roughly a constant fraction of the conversion peak. With a reduced  $\chi_0^2 = 3.8$ , the fit is not perfect, but gives a reliable value for  $\langle n \rangle = (E_0 / \sigma)^2$ , and with it for  $R$ .

In parameter space there are two other local  $\chi^2$  minima of similar depth, which both can be excluded on physics grounds. In one minimum, the backscatter fraction  $f(E)$  has its inflection point  $E_{inv}$  at low energy just where the peak begins to rise, such that almost no backscattered intensity is under the peak, which is very unlikely. The other  $\chi^2$  minimum has  $E_{inv}$  at the high energy end where peak intensity goes to zero again, such that the backscatter fraction is practically constant under the peak, and increases up to 100 percent of all counts at the peak's end, which is equally unlikely.

To investigate the chi-square landscape, fits of a Gaussian with parameters  $n_0, E_0, \sigma$  to the data were done, with the values  $f_0, E_{inv}, w$  for backscatter-subtraction taken from a three dimensional grid, and their  $\chi^2$  calculated. It turned out that the three  $\chi^2$  minima in parameter space are well separated from each other by saddle points that were 20 to 30 units of  $\chi^2$  above the minima. The photoelectron yields at the two false  $\chi^2$  minima were  $R = 253(5)$  p.e./MeV and  $348(8)$  p.e./MeV, 10% and 24% off the central value of  $281(7)$  p.e./MeV at the true minimum, which shows the importance of the backscatter fraction correction. If Eq. (2) is replaced by the similar-looking function  $f(E) = f_0 / 2 \{1 - 2 \arctan[(E - E_{inv}) / w] / \pi\}$ , the three  $\chi^2$  minima are found at the same positions. – This method of backscatter removal from conversion electron lines may be of general interest in electron spectroscopy, where  $^{207}\text{Bi}$  is a standard calibration sources.

## 7. Measurement of photon losses

In order to reduce the number of unknown parameters, the photon loss parameters were measured in a separate experiment with the setup sketched on the left of Fig. 7, see also [40]. The beam of a laser pointer was repeatedly reflected between the two faces of a  $60 \times 60 \times 5$  mm<sup>3</sup> scintillator, (upper panel), or between two reflector foils (lower panel). The number of reflections was varied via the angle of incidence. For each additional reflection, a step appears in the transmission. The transmission of the green light was measured with a  $10 \times 10$  mm<sup>2</sup> photodiode (FDS1010, Thorlabs) coupled directly to a nano amperemeter. At the end of the foil reflectometer, a short piece of acrylic glass was inserted to avoid the bright light reemitted from the scissor-cut end of the reflector foil.

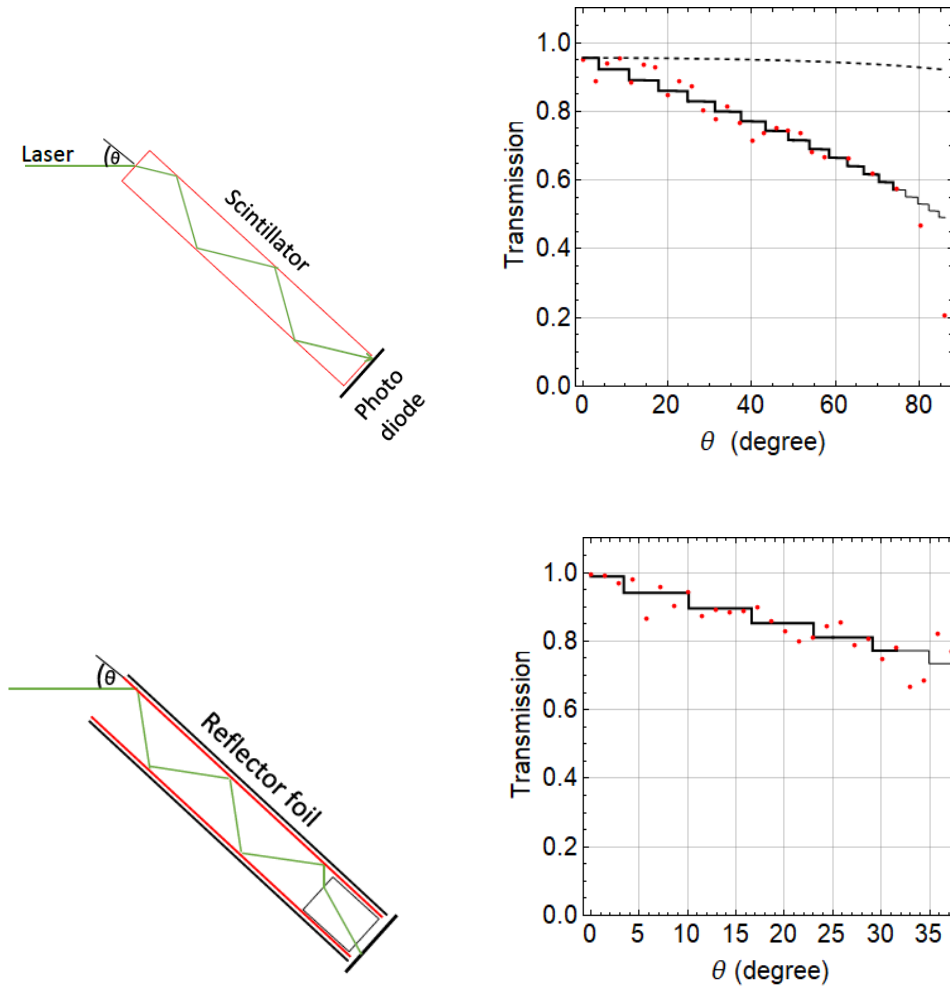


Fig. 7. Measurement of photon losses. Top: Losses upon total reflection. Bottom: Losses on the 3m-ESR reflector foil. Left: Sketches of the apparatus, with reflecting surfaces in red. Right: Measured and calculated photon transmission as a function of the angle of incidence. The thick curves indicate the fit intervals. The upmost dashed curve on the upper right shows the absorption losses in the scintillator, starting at 95% transmission for normal incidence  $\theta = 0^\circ$ .

From the fits of the transmission curves, a reflectivity  $R_t = 96.6(3)\%$  for a single total reflection in the scintillator was obtained, and  $R_f = 95.2(3)\%$  for a single reflection from the reflector foil. In future experiments,  $R_t$  can certainly be improved, because our scintillators showed visible signs of use. In both cases, our assumption of an angle-independent reflectivity was justified a posteriori by the agreement of theory and experiment. The absorption length of the scintillator was determined to 1.3(4) m, the supplier's value being 2.5 m.

## 8. Optimum number of SiPMs

Detection efficiency and the rate of dark counts both depend on the number  $N$  of SiPMs coupled to the scintillator, the first quantity improving, the second deteriorating with increasing  $N$ . A large number of SiPMs is required for the scintillator sizes used in neutron decay experiments, and the question is whether both, reasonable light yield and low detection threshold, can be realized simultaneously. To find out, we measured the yield  $R$  as a function of  $N$  and compared it to expectations. The handling of dark noise will be discussed in the next section.

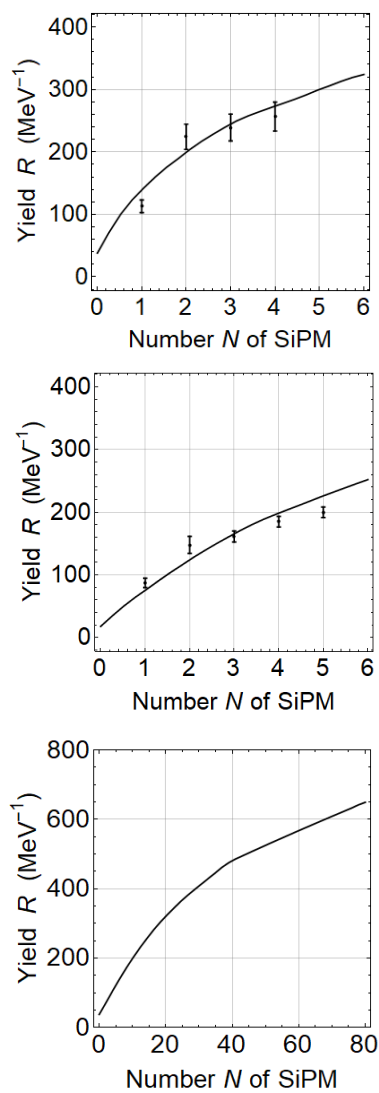


Fig. 8. Yield  $R$  of scintillators of different sizes as a function of the number  $N$  of SiPMs installed. Upper panel for the  $20 \times 20 \times 5 \text{ mm}^3$  plastic scintillator, middle panel for  $40 \times 40 \times 5 \text{ mm}^3$ , lower panel for  $120 \times 120 \times 12 \text{ mm}^3$ , note change of scale. All curves are calculated with the loss parameters obtained in the previous section.

Fig. 8 shows the measured and calculated yields  $R$  for different numbers  $N$  of SiPMs. The measured yields (overvoltage +4.5 V) were obtained from the widths of the 1 MeV  $^{207}\text{Bi}$  conversion line, as described in Sections 5 and 6. Measurements were done for two square plastic scintillator plates of thickness 5 mm, one of  $20\times 20\text{ mm}^2$  area and one of four times this area,  $40\times 40\text{ mm}^2$ , in order to be able to extrapolate to larger areas as they will be needed in neutron decay spectroscopy. An initial light yield of  $Y = 10^4$  photons per MeV electron energy and a SiPM quantum efficiency of  $q = 35\%$  were taken from the data sheets of the suppliers. The photon losses used were those measured in the previous section.

The only free parameter then was an overall device efficiency  $\varepsilon$ . The efficiency needed for agreement with the measured values was  $\varepsilon = 0.44$  for the 20 mm and  $\varepsilon = 0.56$  for the 40 mm wide scintillator. These unaccounted losses can be due, among others, to the mismatch between the refractive indices in the coupling of scintillator and SiPM, which can lead to significant losses, see Fig. 2.21 in Ref. [35].

The errors in Fig. 8 were derived as follows. For a given scintillator-SiPM combination, successive measurements of yield  $R$  gave reproducible results within  $\pm 5\%$  (one sigma), the variation being mainly due to statistics. The observed  $\pm 6.5\%$  variation of  $R$  for different SiPMs is dominated by the unavoidable variations upon a mere reinstallation of a SiPM, and probably not a real effect. The typical error of the spectral fits was only about one half of these variations.  $R$  was also, within  $\pm 6\%$ , independent of overvoltage, in its range from +2.5 V to +5.5 V. From these results an overall error of  $\pm 9\%$  was estimated for the data in Fig. 8. The above variations were found in a long series of test measurements. The data in Fig. 8, on the other hand, were taken all in one final run under identical conditions. After the end of this run it was found that the  $N = 1$  value for the 20 mm wide scintillator was doubtful because the SiPM was sitting on a deteriorated spot, so this value did not receive the same weight as the others.

The bottom panel of Fig. 8 shows  $R(N)$  calculated with the same parameters as in the middle panel, but for a scintillator of size  $120\times 120\times 12\text{ mm}^3$  as required for use with PERC. In this panel,  $N$  is going up to the maximum number of SiPMs that can be accommodated on two opposing edges of the large scintillator, namely,  $N_{max} = 80$  if we take  $6\times 6\text{ mm}^2$  SiPM chips that are now available. The slight kink in the curve for  $N = N_{max}/2$  is due to a shadowing effect of virtual SiPMs by the real SiPMs.

If, instead, all four lateral faces of this scintillator are covered with SiPMs, no reflectors are needed, and photon losses become negligible because the number of total reflections on the large inner faces is limited to five for the given scintillator dimensions. The expected yield then is near  $R = Y (\omega/4\pi) q \varepsilon = 1500 \text{ p.e./MeV}$ , with  $\varepsilon = 0.56$ . This value can probably be increased to 2000 p.e./MeV with a better overall efficiency  $\varepsilon$ . To compare: In present neutron decay experiments, values of up to 500 p.e./MeV are reached when scintillators are read out on all four sides with conventional PMTs, due to additional losses in the light guides and dynodes of the PMT. Calibration spectra obtained with PERKEO are given in [41].

### 9. Suppression of dark counts

A larger number of SiPMs leads to a huge rate of dark counts. In the proposed backscattering experiment of Section 2, only small scintillators are required, and energy resolution can be low because electron backscattering coefficients are only weakly energy dependent. Therefore, a small number of SiPMs per scintillator will be sufficient, and dark counts can be neglected under two- and threefold coincidence. However, in the neutron decay experiments, up to  $N = 160$  SiPMs must be operated in parallel, and the rates of multiple random coincidences of dark counts are so high that they can no longer be blocked by an acceptable discriminator threshold.

But then how can up to  $N = 20\,000$  SiPMs be operated in parallel in the high energy experiments? The solution there is: The signals are counted in multiple coincidence with electron signals coming from other detectors upstream, and are required to fall into a time window  $\Delta t < 100 \text{ ps}$ , so short that hardly any random dark event falls into it. To put it more quantitatively: The rate  $z_n$  of uncorrelated random  $n$ -fold coincidences is given by [42], [43]

$$\frac{z_n}{r_{tot}} \approx n (\Delta t r_{tot})^{n-1}, \quad (3)$$

with the total count rate  $r_{tot}$ . Hence, for small  $\Delta t r_{tot} \ll 1$ , the random coincidence rate can be strongly suppressed. With each additional coincidence,  $z_n$  drops in well measurable steps of width  $E_{1phe} = R^{-1}$  and relative height

$$\frac{z_{n+1}}{z_n} = \frac{n+1}{n} \Delta t r_{tot}. \quad (4)$$

Unfortunately, in neutron decay experiments no such preceding signals are available for coincidence. The proposed solution: multiple coincidences can be required not only with signals from different separate scintillators, but also with signals from a single scintillator, if read out with several detectors. Indeed, most neutron decay experiments listed in the Introduction use several photomultipliers for scintillator readout and require that at least two of them are in coincidence, in order to suppress the small PMT dark rate of typically several kHz. This procedure can be extended to larger numbers of coincidences, which is no problem when we start with a sufficiently high yield  $R \gtrsim 1000$  p.e./MeV of a scintillator fully equipped with SiPMs, as described in the last paragraph of the preceding section. The dark current problem in neutron decay then can be solved in the same way as in the high-energy experiments. Furthermore, in contrast to the high-energy case, neutron decay experiments have extremely low background and do not have the problem of radiation-aging of their detectors.

However, Eqs. (3) and (4) hold only for uncorrelated dark counts, and there remains the problem of correlated dark counts, due to after-pulsing and optical cross talk, which in our SiPMs occur in up to one percent of all pulses. These correlated dark counts may push up the required detector threshold higher than  $nE_{1pbe} = nR^{-1}$  as expected from the above results for uncorrelated coincidences. A large body of literature exists on this topic. The first effect, after pulsing, will be suppressed by the short coincidence window  $\Delta t$ , but only for after pulses with sufficiently long time delay. For the suppression of cross talk, clever methods exist, too, see [44]. In addition, the dark rate can be lowered by disabling individual defective pixels in digital SiPMs [45], though we want to avoid such complicated solutions.

To estimate how serious correlated noise may be, let us have look on the results of  $\gamma$  spectroscopy with SiPM readout. Large NaI scintillators have been read out by arrays of 64 SiPMs of area  $6 \times 6$  mm<sup>2</sup> each, which were found to be mostly free of dark noise above 15 keV [20], [21]. This is highly sufficient for our requirements, because in present neutron decay experiments, fits to the neutron's  $\beta$  spectra begin well above a  $\beta$  energy of 100 keV. Also the linearity of SiPMs will be close to ideal, as neutron decay count rates will be far from saturation. Therefore, one can be optimistic that the problem of correlated noise can also be handled in neutron decay studies with SiPMs.

## 10. Conclusion and outlook

The proposed scintillator-SiPM system is well suited for the planned ToF electron backscatter experiment of Section 2. It will also be interesting for neutron  $\beta$  decay spectroscopy to have a scintillator plate simply equipped with rows of small silicon chips at its edges, with the potential of doubling energy resolution. Further improvement in energy resolution can possibly be obtained with LYSO crystals. Their photon yield is three times that of plastic scintillators, and they are available in sizes of up to  $100 \times 200 \text{ mm}^2$  [46]. Their large refraction index of  $n = 1.83$  increases the usable solid angle of electron emission to  $0.88 \times 4\pi$ , and there exist methods for coping with the resulting refraction mismatch, see references in [47]. With lutetium's high element number  $Z = 71$ , the price to pay are a higher background sensitivity and a larger backscatter fraction. – Many years of work have gone into the scintillator-PMT systems to reach today's high level of precision in neutron decay spectroscopy, and it will certainly take some more years to surpass this level with the proposed SiPM system.

### Summary

The readout of plastic scintillators with SiPMs was studied for use in neutron decay experiments. We shall first use such a system in a ToF-based experiment on electron backscattering, sketched in Fig. 1. A simple tool based on virtual images was developed to model the scintillator-SiPM system, see Fig. 2. A method developed to extract the photoelectron yield from conversion electron signals in the presence of electron backscattering was presented, see Fig. 6. For the plastic scintillator investigated, photon reflection and absorption losses were measured separately, with results shown in Fig. 7. The photoelectron yield expected in a neutron decay experiment with SiPM readout can be estimated from the photon yield measured and calculated as a function of the number of installed SiPMs, given in Fig. 8. Finally, a method to suppress the extreme rates of dark counts in SiPMs is indicated, which will make SiPMs practicable for neutron decay experiments.

### Acknowledgements

I thank S. Bachmann and U. Schmidt from the University of Heidelberg and B. Märkisch from the Technical University Munich for useful discussions.

---

## References

- 1 J.S. Nico and W.M. Snow, Fundamental neutron physics, *Annu. Rev. Nucl. Part. Sci.* 55, 27 (2005).
- 2 H. Abele, The neutron. Its properties and basic interactions, *Progr. Part. Nucl. Phys.* 60, 1 (2008).
- 3 D. Dubbers and M. G. Schmidt, The neutron and its role in cosmology and particle physics, *Rev. Mod. Phys.* 83, 1111 (2011).
- 4 F.E. Wietfeldt and G.L. Greene, The neutron lifetime, *Rev. Mod. Phys.* 83, 1733 (2011).
- 5 M. Tanabashi et al., Particle Data Group, *Phys. Rev. D* 98, 030001 (2018).
- 6 B. Märkisch et al., Measurement of the weak axial-vector coupling constant in the decay of free neutrons using a pulsed cold neutron beam, *Phys. Rev. Lett.* 122, 242501 (2019).
- 7 M.A.-P. Brown, et al., New result for the neutron  $\beta$ -asymmetry parameter  $A_0$  from UCNA, *Phys. Rev. C* 97, 035505 (2018).
- 8 F.E. Wietfeldt et al., aCORN: Measuring the electron-antineutrino correlation in neutron beta decay, *EPJ Web of Conferences* 219, 04008 (2019).
- 9 T.E. Chupp et al., Search for a T-odd, P-even triple correlation in neutron decay, *Phys. Rev. C* 86, 035505 (2012).
- 10 A. Kozela et al., Measurement of the transverse polarization of electrons emitted in free neutron decay, *Phys. Rev. C* 85, 045501 (2012).
- 11 X. Wang, et al., Design of the magnetic system of the neutron decay facility PERC, *EPJ Web of Conferences* 219, 04007 (2019).
- 12 K. Bodek et al., BRAND – Search for BSM physics at TeV scale by exploring transverse polarization of electrons emitted in neutron decay, *EPJ Web of Conferences* 219, 04001 (2019).
- 13 D. Dubbers, Magnetic guidance of charged particles, *Phys. Lett. B* 748 (2015) 310.
- 14 D. Dubbers and U. Schmidt, Generation of narrow peaks in spectroscopy of charged particles, *Nucl. Instrum. Methods A* 837,50 (2016).
- 15 C. Roick, D. Dubbers, B. Märkisch, H. Saul, and U. Schmidt, Electron time-of-flight: A new tool in  $\beta$ -decay spectroscopy, *Phys. Rev. C* 97, 035502 (2018).
- 16 A.N. Otte and D. Garcis, A very brief review of recent SiPM developments, *PoS(PhotoDet2015)001*.
- 17 F. Acerbi and S. Gundacker, Understanding and simulating SiPM, *Nucl. Instrum. Methods A* 926, 16 (2019).
- 18 R. Klanner, Characterisation of SiPMs, *Nucl. Instrum. Methods A* 926, 36 (2019).
- 19 F. Simon, Silicon photomultipliers in particle and nuclear physics, *Nucl. Instrum. Methods A* 926, 85 (2019).
- 20 Zhenhua Lin, Benoit Hautefeuille, Sung-Hee Jung, Jinho Moon, and Jang-Guen Park, The design of a scintillation system based on SiPMs integrated with gain correction functionality, *Nucl. Eng. and Techn.* 52, 164 (2020).
- 21 C. Mihai et al., Development of large area Silicon Photomultipliers arrays for  $\gamma$ -ray spectroscopy applications, *Nucl. Instrum. Methods A* 953, 163263 (2020)
- 22 M.T. Hassan et al., The aCORN backscatter-suppressed beta spectrometer, *Nucl. Instrum. Methods A* 867, 51 (2017).
- 23 C. Roick, H. Saul, H. Abele, and B. Märkisch, Undetected electron backscattering in PERKEO III, *EPJ Web of Conferences* 219, 04005 (2019).
- 24 B. Plaster et al., Final result for the neutron  $\beta$ -asymmetry  $A_0$  from the UCNA experiment, *EPJ Web of Conferences* 219, 04004 (2019).
- 25 J.W. Martin, et al., New measurements and quantitative analysis of electron backscattering in the energy range of neutron  $\beta$ -decay, *Phys. Rev. C* 73, 015501 (2006).
- 26 V.V. Golovko, V.E. Iacob, and J.C. Hardy, The use of Geant4 for simulation of a plastic  $\beta$ -detector and its application to efficiency calibration, *Nucl. Instrum. Methods A* 594, 266 (2008).
- 27 Geant4, a simulation toolkit, <http://geant4.web.cern.ch/geant4/>

- 
- 28 PENELOPE2018, A Code System for Monte-Carlo Simulation of Electron and Photon Transport, <https://www.oecd-nea.org/tools/abstract/detail/nea-1525/>
- 29 D. Dubbers, Characterization of electron detectors by time-of-flight in neutron  $\beta$ -decay experiments, arxiv 1611.00192.
- 30 J.D. Jackson, S.B. Treiman, and H.W.Jr. Wyld, *Phys. Rev.* 106, 517 (1957).
- 31 F. Glück, I. Jo6, and J. Last, Measurable parameters of neutron decay, *Nucl. Phys. A* 593, 125 (1995).
- 32 N. Severijns, M. Beck, and O. Naviliat-Cuncic, 2006, "Test of the Standard Electroweak Model in Beta Decay", *Rev. Mod. Phys.* 78, 991-1040.
- 33 G. Keil, Design principles of fluorescence radiation converters, *Nucl. Instrum. Methods* 89, 111 (1970).
- 34 E. Roncali, M. Amin. Mosleh-Shirazi, and A. Badano, Modelling the transport of optical photons in scintillation detectors, *Phys. Med. Biol.*, 62(20), R207 (2017).
- 35 C. Roick, doctoral thesis, <https://mediatum.ub.tum.de/doc/1452579> (2018).
- 36 P.W.Cattaneo and A.Schöning, MEG II and Mu3e status and plan, *EPJ Web of Conferences* 212, 01004 (2019).
- 37 H. Klingemeyer, Y. Munwes, K. Briggel, T. Zhong, H. Chen, W. Shen, and H.-C. Schultz-Coulon, Measurements with the technical prototype of the Mu3e tile detector, *Nucl. Instrum. Methods A* 958, 162852 (2020).
- 38 L. Gruber, S.E. Brunner, J. Marton, H.Orth, and K. Suzuki, Barrel time-of-flight detector for the PANDA experiment at FAIR, *Nucl. Instrum. Methods A* 824, 105 (2016).
- 39 F. Sefkow and F. Simon, A highly granular SiPM-on-tile calorimeter prototype, *J. Phys. Conf. Ser.* 1162 01, 2012 (2019)
- 40 G. Kettenring, Measurement of the reflectivities and absorption lengths at different wavelengths of plastic scintillator and acrylicglass, *Nucl. Instrum. Methods* 131, 451 (1975).
- <sup>41</sup> H. Saul, C. Roick, H. Abele, H. Mest, M. Klopff, A.K. Petukhov, T. Soldner, X. Wang, D. Werder, and B. Märkisch, Limit on the Fierz Interference Term  $b$  from a Measurement of the Beta Asymmetry in Neutron Decay, *Phys. Rev. Lett.* 125, 112501 (2020).
- 42 L. Jánossy, Rate of  $n$ -fold accidental coincidences, *Nature* 153, 165 (1944).
- 43 E. Schrödinger, Rate of  $n$ -fold accidental coincidences, *Nature* 153, 592 (1944).
- 44 A.Stoykov, J.-B.Mosset, U.Greuter, M.Hildebrandt, and N.Schlumpf, A SiPM-based ZnS:6LiF scintillation neutron detector, *Nucl. Instrum. Methods A* 787, 361 (2015).
- 45 Z. Liu, M. Pizzichemi, E. Auffray, P. Lecoqband, and M. Paganonia, Performance study of Philips digital silicon photomultiplier coupled to scintillating crystals, 2016 JINST 11 P01017
- 46 <http://www.shalomeo.com>
- 47 F. Liu et al., Large energy resolution improvement of LYSO scintillator by electron beam lithography method, *AIP Advances* 10, 025101 (2020).